

4. Historical overview of the development of scanning BRILLOUIN microscopy

A comprehensive overview of the historical development of scanning BRILLOUIN microscopy (SBM) is presented below. In sections 4.1 to 4.5 some early illustrative examples of SBM experiments performed by our own research group will demonstrate the scientific broadness of the application area of this technique.

First steps towards SBM were made in the late 1970s, although these spatially resolving BRILLOUIN spectroscopic investigations were not denoted as such (KRÜGER & UNRUH 1977). At these days, SBM was used to probe the spatial decay of the density of states of microwave induced acoustic phonons in quartz crystals (KRÜGER & UNRUH 1977) (see section 4.1). About 10 years later, in 1988 a point sampling BRILLOUIN microscopy technique combined with angle-resolved BRILLOUIN spectroscopy was developed by the KRÜGER group (MARX *et al.* 1988). These studies aimed at the determination of the temperature dependence of the full elastic tensor characterizing small crystalline grains of melt-crystallized perfluoroalkanes and difluorotetrachloroethane (MARX *et al.* 1988, 1989, KRÜGER *et al.* 1994). For these investigations the spatial scanning facility was of minor importance. The first 'real' SBM studies, combining an important focusing of the incident laser beam on the sample with spatial scanning of the scattering volume, were accomplished in the θA scattering geometry and reported in 1987 for uniaxially stretched poly(methylmethacrylate) polymers (PEETZ 1987) (see section 4.3). The aim of these measurements was to get deeper insight into the relationship between the molecular orientation induced by a mechanical stretching process and the thereby created acoustic anisotropy and spatial inhomogeneity of the specimen (PEETZ 1987, KRÜGER 1989). This study yielded the first two-dimensional hypersonic profiles. However due to the small number of data points the latter did hardly correspond to two-dimensional hypersonic mapping. In 1990 SBM ^{θA} gave access to the evolution of acoustic profiles as a function of the ionic concentration in sodium cyanide and sodium chloride mixed crystals $\text{NaCN}_x\text{Cl}_{1-x}$ (JIMÉNEZ RIOBÓO *et al.* 1990, KRÜGER *et al.* 1990) (see section 4.2). These profiles could be related to the ferroelastic and quadrupolar glass transitions of the mixed crystals.

TAKAGI and KURIHARA (1992) were the first to develop a confocal SBM¹⁸⁰ setup. The related article (TAKAGI & KURIHARA 1992) mainly characterised the innovative aspect of a confocal BRILLOUIN setup derived from RAMAN microscopy. A spatial resolution of about 1 μm was realized, but the restrictions given by the backscattering geometry represented a major drawback (see section 3.2). First applications of the confocal SBM¹⁸⁰ technique to polymer films and acoustic surface waves of aluminium films could be demonstrated (TAKAGI & KURIHARA 1992). Point sampling BRILLOUIN microscopy, using similar setups as the SBM¹⁸⁰ setup proposed by TAKAGI and KURIHARA, was applied by different research groups to various materials ranging from ferroelastic materials like paratellurite to biological materials like bone and hen egg white lysozyme (e.g. AHART *et al.* 1996, 1999, ZHA *et al.* 1996, JIANG & KOJIMA 2000, KIM *et al.* 2005, BRETOS *et al.* 2007, SAKAMOTO *et al.* 2008, SVANIDZE *et al.* 2009, HASHIMOTO *et al.* 2010, JIMÉNEZ RIOBÓO *et al.* 2010). In these studies, commercial confocal microscopes were usually used to focus the laser beam and to collect the inelastically scattered light. A spatial scanning facility was in general of minor or of no importance at all for these studies.

In 1994, KRÜGER *et al.* (1994) used SBM ^{θA} as a tool to assess the position and size of optically irresolvable crystal grains in polycrystalline films (see section 4.4). A further innovative application of SBM ^{θA} was published in 2000, namely the possibility to directly probe internal stress fields within solids (KRÜGER *et al.* 2000, 2001) (see section 4.5).

During the last ten years SBM has become a more current experimental tool. SBM ^{θA} was improved in such a way to attain a spatial resolution of about 1 μm (SANCTUARY *et al.* 2003). Thus SBM ^{θA} became from the viewpoint of resolution equivalent to SBM¹⁸⁰, without suffering from the restrictions given by the backscattering geometry. Especially elastic indicatrices could be measured with high spatial resolution using the θA scattering geometry. This technique permitted to probe so-called interphases in semi-crystalline and amorphous polymers (SANCTUARY *et al.* 2003, KRÜGER *et al.* 2004a, 2005) (see chapter 5). In addition to interphases, spatial morphological heterogeneities caused by polymerization were

explored by means of SBM^{0A} in thin epoxy films deposited on gold, copper and aluminium substrates (POSSART *et al.* 2006, WEHLACK *et al.* 2007). In 2004 the HILLEBRANDS group developed a high resolution SBM¹⁸⁰ technique to probe the spatial distributions of magnons (DEMIDOV *et al.* 2004, PERZLMAIER *et al.* 2005, SANDWEG *et al.* 2008). At the same time, SBM^{0A} was adapted so as to investigate microwave-induced surface and bulk acoustic field distributions created by non-resonant interdigital structures deposited on different piezoelectric substrates (see section 4.1) (KRÜGER *et al.* 2004b, VINCENT *et al.* 2005a, 2005b, MURATA *et al.* 2007, YOSHIDA *et al.* 2008). In 2005, KOSKI & YARGER (2005) presented the first two-dimensional hypersonic frequency map, recorded for a polystyrene-methanol interface using SBM¹⁸⁰. In 2007 the BRILLOUIN microscopy technique proposed by TAKAGI & KURIHARA (1992) was practically reinvented by LIPTAK *et al.* (2007), who used a modified ZEISS microscope as the focusing and collecting optics. Moreover, different SBM techniques adapted for the investigation of biomaterials were proposed (SCARCELLI & YUN 2008, SO 2008). Only recently a combined space- and time-resolved BRILLOUIN spectroscopic technique, SBM^{180-2D} (see section 3.2), has demonstrated its power for mapping matter transport and structure formation processes at unstable interfaces between solids and liquids (see chapter 5) as well as between two liquids (see chapter 6) (SANCTUARY *et al.* 2009, 2010, PHILIPP *et al.* 2009, 2011).

4.1. Hypersonic mapping of microwave-induced hypersonic waves

According to our knowledge the first SBM investigations were performed in the late 1970s in the context of microwave induced phonons (KRÜGER & UNRUH 1977, KRÜGER *et al.* 1978b). At that time the spatial sound attenuation at high frequencies in quartz crystals was in the focus of basic research (KRÜGER & UNRUH 1977). However, adequate pulse-echo based ultrasound techniques were not available in the GHz-range. The alternative technique, BRILLOUIN spectroscopy, in principle yields access to the temporal hypersonic attenuation Γ_t (s^{-1}) in the GHz range by

considering the width of the involved BRILLOUIN line. (Note that the index ‘t’ is only used here in order to discriminate between the temporal and spatial hypersonic attenuation.) In case of moderate acoustic attenuation, the spatial acoustic attenuation Γ_{y_1} (m^{-1}) is given by $\Gamma_{y_1} = \frac{1}{v} \Gamma_t$ with v denoting the sound velocity of an excited acoustic wave propagating along y_1 . However, due to the limited finesse of the BRILLOUIN spectrometers in the 1970’s, it was impossible to derive the very small temporal attenuation from the width of the related BRILLOUIN line (KRÜGER & UNRUH 1977).

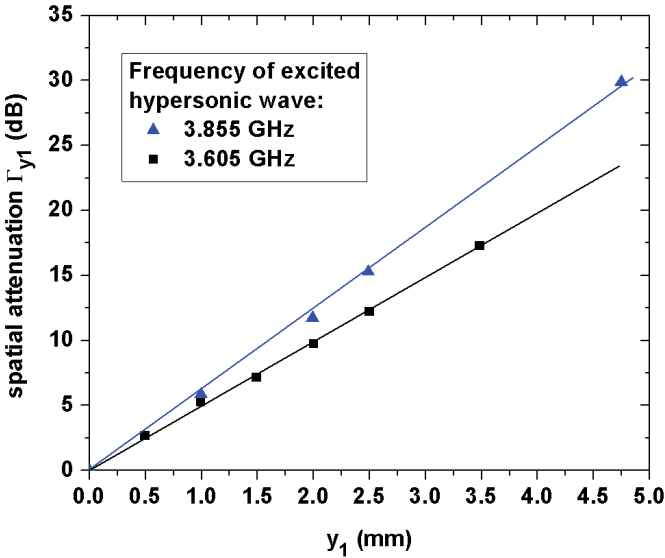


Fig. 4.1. Spatial hypersonic attenuation Γ_{y_1} versus distance y_1 for two longitudinally polarized hypersonic waves excited at two slightly differing frequencies.

Hereupon an innovative technique was introduced, which consisted in inducing coherent hypersonic waves in piezoelectric quartz crystals placed in a microwave cavity (KRÜGER & UNRUH 1977). The spatial attenuation of the microwave-induced acoustic wave could be directly accessed by probing the spatial

decrease of the intensity of the related BRILLOUIN line (see figure 2.1 in section 2.1). The experimental setup was similar to that of figure 3.3, except that the external transducer which is not needed for a piezoelectric material like quartz was omitted. Instead, hypersonic bulk waves were excited at the (y_2, y_3) -surface of a quartz crystal in an half open (quarter wavelength) microwave resonator with the energy propagating along $\bar{y}_1 = \bar{x}_1$, i.e. the phonon wave vector \bar{q} being collinear to \bar{y}_1 . By selecting an adequate scattering setup so that the sampled phonon wave vector is collinear to \bar{y}_1 , the SBM^{θA} technique permits to scan the intensity of the microwave-induced phonon versus y_1 (KRÜGER & UNRUH 1977). It turns out that the amplitude of the induced bulk acoustic wave exponentially diminishes versus distance y_1 from the electro-acoustically excited surface of the quartz crystal. Figure 4.1 shows the related spatial attenuation data versus distance curves for sound waves excited at two slightly differing hypersonic frequencies. The origin of the \bar{y}_1 -axis is located at the surface of the quartz crystal. Note that from a technical viewpoint rather the spatial scanning facility than a high spatial resolution was needed for this study.

More recently the SBM^{θA} technique enabled the characterization of the field distribution of surface acoustic waves generated by interdigital transducers (KRÜGER *et al.* 2004b, VINCENT *et al.* 2005a, 2005b). Such surface acoustic wave devices are commonly used for the conversion of electric energy into mechanical energy, and vice versa, in filter, oscillator and transformer systems (BÖMMEL & DRANSFELD 1960, DE KLERK 1976). Typical applications for surface acoustic wave devices are mobile phones. Figure 4.2 shows the schematic representation of a surface acoustic wave device based on a lithium niobate crystal suitably cut for the excitation of purely longitudinally polarized acoustic modes at microwave frequencies. The interdigital structure acting as a microwave source generates acoustic surface and bulk waves within the piezoelectric substrate on which it is deposited. In case of a well-considered design of the source interdigital structure, these waves propagate along \bar{x}_1 . It has to be stressed that the mapping of the created acoustic fields is an absolute prerequisite for a better understanding and an improvement of the technology of surface acoustic wave devices. Indeed, the

resolution of the acoustic field distribution allows for evaluating the suitability of the microwave source. Moreover, the working principle of the receiver of the surface acoustic wave device also needs further elucidation. However, until the end of the last decade, only an indirect visualisation of the acoustic field distribution was achieved, e.g. by optical interferometry, atomic force microscopy, and x-ray spectroscopy (WHATMORE *et al.* 1982, MONCHALIN 1985, BEHME & HESJEDAL 2001).

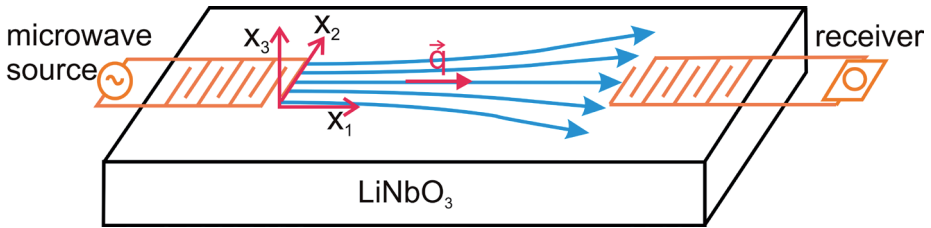


Fig. 4.2. Schematic representation of the surface acoustic wave device with interdigital structures (in orange) deposited on a lithium niobate plate. In blue: microwave-induced acoustic field with wave vector \vec{q} ; $\{x_1, x_2, x_3\}$: sample coordinate system.

In 2004 KRÜGER *et al.* (KRÜGER *et al.* 2004b) succeeded in characterizing the spatial decay of surface and bulk acoustic waves generated by the 1 mm broad emitting interdigital finger structure deposited on lithium niobate (LiNbO_3). Figure 4.3 shows typical BRILLOUIN spectra recorded in between the microwave source and the receiver. The black curve corresponds to the case when there is no microwave excitation, whereas the red spectrum was recorded while microwave-induced acoustic waves were propagating along \bar{x}_1 . The position of the intense Anti-STOKES line (in red) in the BRILLOUIN spectrum shows that a longitudinally polarized sound wave was generated. As the spectral scattering intensity axis is given on a logarithmic scale, the intensity of that BRILLOUIN line exceeds that of its thermal counterpart by a factor of greater than 300. Amplifications of the intensity of thermal acoustic phonons by a factor of 10^7 are commonly realized. Figure 4.3

clearly reveals that the microwave generation of acoustic phonons is, in general, a powerful technique to intensify thermally excited acoustic phonons within materials possessing small opto-acoustic coupling coefficients (NYE 1972, VACHER & BOYER 1972). Adjusting the microwave frequency carefully with a frequency counter until the maximum intensity of the related BRILLOUIN line is achieved permits to determine the phonon frequency even with huge accuracy.

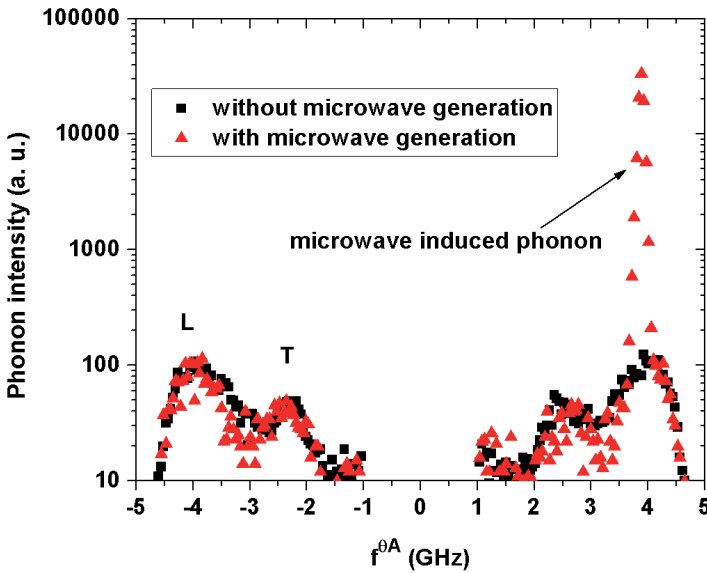


Fig. 4.3. BRILLOUIN spectra of thermally excited longitudinally (L) and transversely (T) polarized acoustic modes and of a microwave-induced longitudinally polarized acoustic phonon.

In order to access the acoustic field distribution of the microwave induced surface and bulk waves, the scattering volume is scanned along \bar{x}_1 and \bar{x}_2 on the surface and within the bulk of the lithium niobate plate using SBM^{θA} (VINCENT *et al.* 2005a). The general shape of the surface acoustic field distribution depicted in figure 4.4 agrees well with theoretical predictions given in (VINCENT *et al.* 2005a). The spatial attenuation of the surface acoustic wave and the bulk acoustic wave (not

shown) along \bar{x}_1 is consistent with literature data (VINCENT *et al.* 2005a). The width of the acoustic field corresponds well to that of the microwave source without a significant spreading for increasing x_1 -values. Hence up to $x_1 = 2.1$ mm no relevant fanning out of the phonon wave vector occurs. This feature is of course highly desired for surface acoustic wave devices, for which the whole acoustic field intensity should be recorded by the receiver. This fascinating application of BRILLOUIN mapping of induced acoustic fields was picked up in 2007 by the group of MATSUKAWA (MURATA *et al.* 2007, YOSHIDA *et al.* 2008).

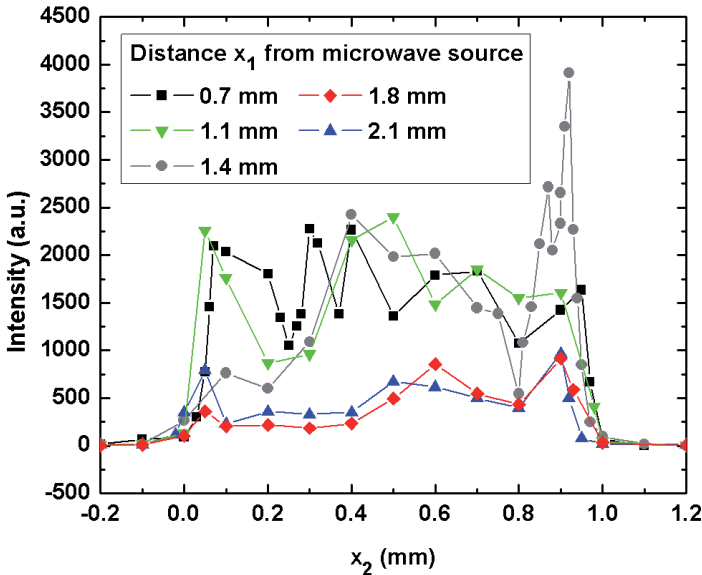


Fig. 4.4. Two-dimensional intensity map of the BRILLOUIN line related to the surface acoustic wave.

4.2. Influence of compositional disorder on the shear modulus of a mixed crystal

As argued in chapter 3, SBM^{θA} is a really versatile technique to study spatially varying morphologies by exploring the related elastic property profiles. Structural inhomogeneities or heterogeneities can be probed by spatial and, if necessary, by

additional angular scans of the hypersonic velocity and attenuation. An early, most fascinating SBM^{0A} study concerned morphologically inhomogeneous materials, namely sodium cyanide and sodium chloride mixed crystals $\text{NaCN}_x\text{Cl}_{1-x}$, with x denoting the CN^- fraction (JIMÉNEZ RIOBÓO *et al.* 1990, KRÜGER *et al.* 1990). A so-called critical concentration $x_c = 0.65$ exists for this crystalline material: for $x > x_c$, $\text{NaCN}_x\text{Cl}_{1-x}$ shows a ferroelastic phase transition below room temperature and for $x \leq x_c$ the ferroelastic transition changes to a quadrupolar glass transition (SALJE 1990, KRÜGER *et al.* 1990, JIMÉNEZ RIOBÓO *et al.* 1990). Pure sodium chloride undergoes no phase transition at all close to room temperature. The first order ferroelastic transition is moreover accompanied by a strong critical behaviour (JIMÉNEZ RIOBÓO *et al.* 1990, KRÜGER *et al.* 1990, SALJE 1990).

The used CZOCHRALSKI growth procedure leads to $\text{NaCN}_x\text{Cl}_{1-x}$ single crystals with compositional changes in every direction of space. Despite their morphological inhomogeneity, these mixed crystals maintain cubic symmetry in their room temperature phase. Figure 4.5a schematically depicts such a large melt-grown $\text{NaCN}_x\text{Cl}_{1-x}$ single crystal, with a typical diameter of 30 mm and a length of 100 mm. As illustrated in figure 4.5b the large crystal is cut in parallel, about 2 mm thick crystal slices, so that the \bar{x}_3 -axis of each slice is collinear to that of the large single crystal. Similar to the large crystal, every slice shows continuous compositional variations in every direction. But surprisingly, a unique and sharp ferroelastic phase transition at a temperature T_c (SALJE 1990) is observed for each slice. The ferroelastic phase transition temperature however varies from slice to slice. Apparently, in a continuous crystal plate a kind of spatial self-averaging of the transition temperature $T_c = \langle T_c(\vec{r}) \rangle_{\vec{r}}$ happens, leading to a unique and sharp phase transition per slice, even if significant compositional gradients exist therein. As the shear modulus c_{44} is the order parameter susceptibility of the ferroelastic phase transition, and hence is intimately related to the transition temperature T_c , the question appears whether the same self-averaging happens for the shear modulus $c_{44} = \rho \cdot v_T^2$ (KRÜGER *et al.* 1990). In this context it suffices to determine the purely transversely polarized sound velocity v_T , since the influence of the mass density ρ on the shear modulus can be neglected compared to the acoustic contribution v_T^2 .

In a first step the acoustic indicatrix within the slice’s plane was constructed in order to determine the pure mode axis \bar{y}_1 ; note that angle-resolved SBM^{0A} is absolutely required for this investigation. Figure 4.6 depicts the obtained indicatrix with the three sound velocity modes, from which the pure mode direction \bar{y}_1 can be assigned (KRÜGER *et al.* 1990). Remark that the elements of the elastic tensor can be determined by a least squares fit of the measured data using a projection of the CHRISTOFFEL equation (see section 2.4 and (AULD 1973)) on a cubic plane, the (y_1, y_2) -plane:

$$v_{qL, qT} = \sqrt{\frac{c_{11} + c_{44} \pm \sqrt{(c_{11} - c_{44})^2 \cdot \cos^2(2\Phi) + (c_{12} + c_{44})^2 \sin^2(2\Phi)}}{\rho}} \quad (4.1)$$

and
$$v_T = \sqrt{\frac{c_{44}}{\rho}}, \quad (4.2)$$

where Φ designates the angle between the phonon wave vector \bar{q}^{90A} and the \bar{y}_2 axis. The ‘+’ sign in front of the inner square root designates the quasi-longitudinally polarized mode (qL), while the ‘-’ denotes the quasi-transversely polarized mode (qT).

The third mode is purely transversely polarized and hence designated by ‘T’ in equation (4.2). The corresponding fit curves are given as red lines in figure 4.6. Fixing the x_1 -trace defined in figure 4.5b along the experimentally determined \bar{y}_1 -direction easily gives access to the $v_T(y_1)$ -dependence. The obtained result given in figure 4.5c is really striking: a self-averaging of $v_T(y_1)$, respectively of $c_{44}(y_1)$, does not take place. In other words, whereas the phase transition temperature $T_c(\bar{r})$ self-averages in some way over the composition of a contiguous crystalline slice, the shear modulus $c_{44}(y_1)$, being the phase transition-related order parameter susceptibility does not. The above discussion clearly reveals that **SBM permits to give a unique perspective on the relationship between the elastic properties and compositional disorder of mixed crystals, as well as the related phase transition behaviour.**

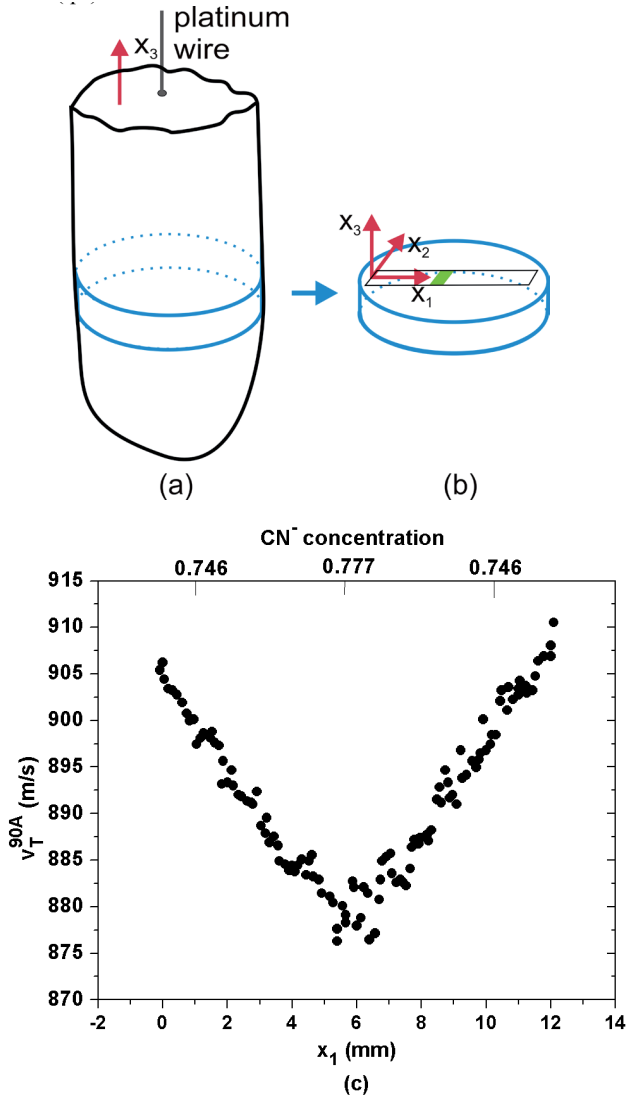


Fig. 4.5. (a) Sketch of a CZOCHRALSKI grown single crystal of $NaCN_xCl_{1-x}$, hanging on a platinum wire. (b) Studied crystal slice. The scattering volume V (only depicted in green in two-dimensions) is scanned along \vec{x}_1 . $\{x_1, x_2, x_3\}$: sample coordinate system. (c) Sound velocity v_T^{90A} of a transversely polarized mode measured as a function of $x_1 = y_1$ along the crystal slice depicted in (b).

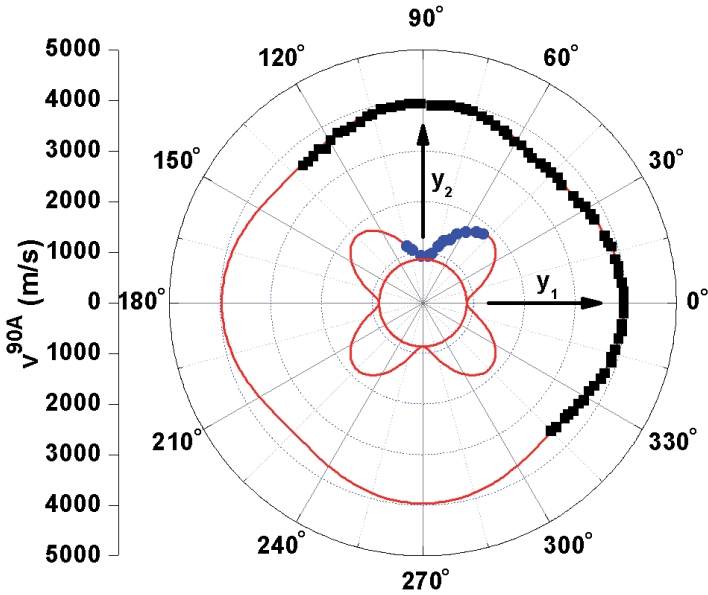


Fig. 4.6. Acoustic indicatrix for the (y_1, y_2) -plane within one crystal slice. Black squares: quasi-longitudinally polarized mode, blue dots: one quasi-transversely polarized mode. In red: fit curves using the CHRISTOFFEL equation for cubic symmetry. (y_1, y_2, y_3) : symmetry coordinate system.

4.3. Spatially distributed acoustic anisotropies in polymers provoked by uniaxial stretching

The technological relevance of molecularly oriented polymers, like high-modulus fibres, stems amongst others from the significantly increased elastic modulus along the direction of tension, compared to the isotropic state of the polymer (WARD 1971, 1975, MARK *et al.* 2004). In the focus of research is the relation between the tensile conditions (degree of stretching, temperature, etc.) and the achieved molecular bond orientation which is strongly correlated to the elastic property improvement (WARD 1971, 1975). During uniaxial stretching of an initially isotropic polymeric sample, symmetry-breaking occurs and may lead to fibre symmetry or to orthorhombic

symmetry. In molecularly oriented amorphous and semi-crystalline polymers, the symmetry of the elastic tensor may even vary in space. This property is in clear contrast to the observations made in the previous section 4.2, where an identical symmetry was noticed for the whole morphologically inhomogeneous sample. In the following the elastic tensor properties versus degree of stretching, as well as the spatial evolution of the elastic moduli are elucidated for different polymers.

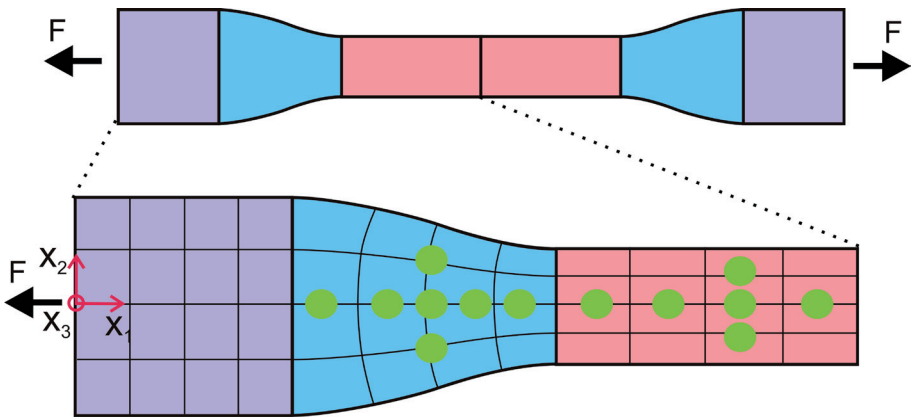


Fig. 4.7. Schematic representation of a polymeric sample after uniaxial stretching along \bar{x}_1 . F : tensile force, green spots: typical positions for the scattering volume. $\{x_1, x_2, x_3\}$: sample coordinate system.

Figure 4.7 schematically indicates the shape of the polymeric sample after uniaxial stretching along the \bar{x}_1 -direction (PEETZ 1987). The wider end parts of the sample, marked in magenta, indicate where the clamps were placed to transmit the load \vec{F} to the sample. For the studied polymers, the experiments were performed in such a way that these parts do neither molecularly orient nor shrink upon uniaxial deformation. Prior to the experiment, the shape of the specimen is chosen such that a so-called neck starts to develop in the middle of the sample upon stretching and migrates towards both wider ends for an increasing degree of stretching. Within the neck both

molecular flow and orientation happen (WARD 1971, PEETZ 1987). As shown in figure 4.7 for large degrees of stretching the neck, marked in blue, is finally positioned adjacent to the end parts of the specimen. The molecular texture developing during the stretch process in the middle of the sample (marked in red) is roughly fibre symmetric, with the axis of stretching x_1 corresponding to the fibre axis y_1 (PEETZ 1987, KRÜGER 1989).

In a first step, the influence of this molecular orientation around the fibre axis on the linear elastic properties is recorded using angle-resolved SBM^{θA}, with the fixed scattering volume being placed within the middle (see red part in figure 4.7) of a poly(ethylene terephthalate) (PET) sample (PEETZ 1987, KRÜGER 1989). The sound velocity of the longitudinally polarized mode, and hence the elastic modulus c_{11} , are known to significantly increase along the tensile force direction for increasing degrees of stretching (PEETZ 1987, KRÜGER 1989, WARD 1971). The experiment was carried out as follows: the semi-crystalline PET specimen with an initial degree of crystallinity of 27% was stretched at a temperature which lies 3 K above its glass transition temperature and then quickly cooled down to conserve the strain (PEETZ 1987). Thereby a maximal degree of crystallinity of 36% was reached for the highest degree of stretching (of six). Using angle-resolved SBM^{θA}, sound velocity indicatrices within the (x_1, x_2) -plane could be constructed for nine different degrees of stretching (between one and six). The phonon wave vector \vec{q}^{90A} hence rotated in the (x_1, x_2) -plane for a given position of the scattering volume in the middle of the specimen. The corresponding datasets for the quasi-longitudinally and quasi-transversely polarized phonon mode are indicated in figure 4.8. The solid lines in figure 4.8 are fitted curves using the appropriate eigenvalues derived from the CHRISTOFFEL equation for orthorhombic symmetry (AULD 1973) in the (y_1, y_2) -symmetry plane:

$$v_{qL, qT} = \sqrt{\frac{c_{66} + c_{11} \cos^2 \Phi + c_{22} \sin^2 \Phi \pm \sqrt{(c_{66} + c_{11} \cos^2 \Phi + c_{22} \sin^2 \Phi)^2 - 4C}}{2\rho}} \quad (4.3)$$

with

$$C = (c_{11} \cos^2 \Phi + c_{66} \cos^2 \Phi) \cdot (c_{66} \cos^2 \Phi + c_{22} \cos^2 \Phi) - (c_{12} + c_{66})^2 \cos^2 \Phi \cdot \sin^2 \Phi$$

and

$$v_T = \sqrt{\frac{c_{44} \cos^2 \Phi + c_{55} \sin^2 \Phi}{\rho}}, \quad (4.4)$$

where $v_{qL, qT}$ denote the quasi-longitudinal ('+' sign in front of the inner square root) and the quasi-transverse ('-' sign in front of the inner square root) modes for orthorhombic symmetry. Values corresponding to the transversely polarized acoustic mode are not indicated. The values of the tensor components $c_{11}, c_{22}, c_{44}, c_{55}, c_{66}$ and c_{12} are obtained from fitting equations (4.3) and (4.4) to the measured datasets of figure 4.8 (PEETZ 1987). The sound velocity value v_{qL} of the quasi-longitudinally polarized phonon almost doubles and hence the effective modulus increases by almost a factor of 4 along \bar{x}_1 during the tensile experiment. Moreover, the relative change of v_{qL} is obviously the strongest along the direction of tension. This is usually interpreted in terms of covalent bond alignment, or polymeric chain alignment along the \bar{x}_1 -direction (WARD 1971, 1975). Along x_2 , i.e. orthogonally to the direction of tension, v_{qL} and hence the effective modulus, even slightly decrease. In fact, as the polymeric chains orient in the x_1 -direction, the average number of covalent bonds oriented along the x_2 -direction decreases while that of much weaker intermolecular VAN DER WAALS bonds increases (WARD 1971, 1975). In total, this leads to a decrease of the longitudinally polarized sound velocity perpendicular to the direction of tension.

As a complement to the above discussed angle-resolved BRILLOUIN spectroscopic study, sound velocities were spatially resolved within the (x_1, x_2) -plane of both the neck and the middle parts for a fixed phonon wave vector \bar{q}^{180} parallel to \bar{x}_3 . These SBM¹⁸⁰ studies were carried out on uniaxially oriented amorphous poly(methylmethacrylate) samples having the shape given in figure 4.7 (PEETZ 1987, KRÜGER 1989). While figure 4.9a shows the evolution of the sound velocity profile along the direction of tension \bar{x}_1 , figure 4.9b depicts v_L^{180} versus x_2 . The respective experiments were carried out for an identical high degree of stretching.

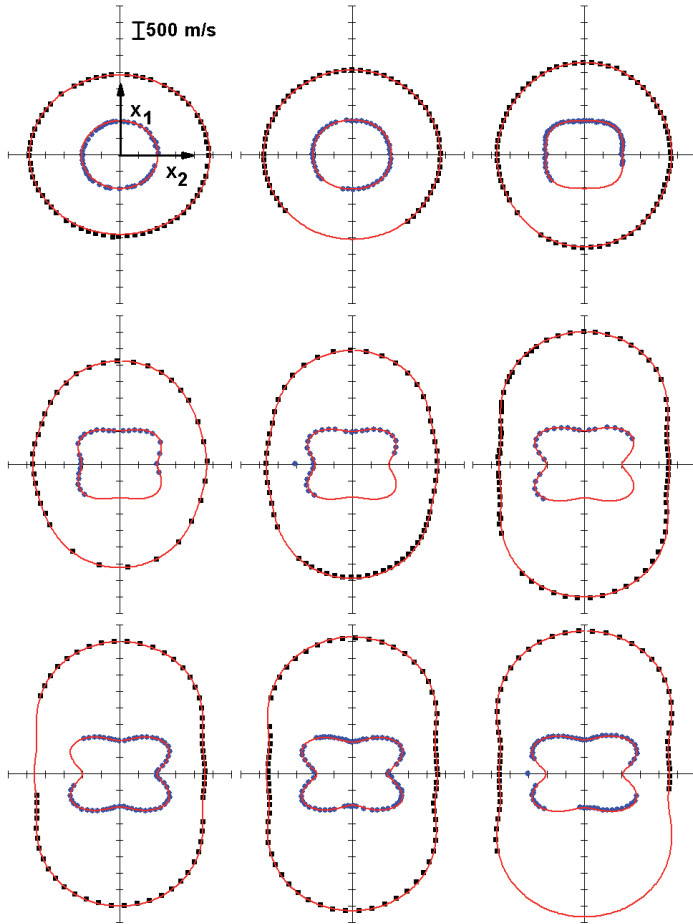


Fig. 4.8. Indicatrices for the quasi-longitudinally (in black) and quasi-transversely (in blue) polarized phonon mode obtained for nine different states of a PET specimen uniaxially stretched along x_1 . Red curves: fits using the CHRISTOFFEL equation.

The longitudinal sound velocity lowering between the necks and the middle part of the stretched specimen (see figure 4.9a) is consistent with a high molecular orientation along x_1 in the middle part of the sample. As discussed above, this molecular orientation along x_1 leads to a longitudinal sound velocity decrease along

both the \bar{x}_2 and \bar{x}_3 directions as a depletion of covalent bonds along the latter directions is only partially compensated by the increase of weaker interchain VAN DER WAALS bonds.

The sound velocity scans performed in the \bar{x}_2 -direction, shown in figure 4.9b, confirm that the mechanical deformation of the specimen is homogeneous perpendicular to the direction of stretching \bar{x}_1 . Hence, even in the neck the stretched sample does not only show optical homogeneity (PEETZ 1987), but also elastic homogeneity perpendicular to the direction of stretching. In summary, on a phenomenological level SBM is a highly versatile technique for the characterization of the state of molecular orientation within polymers as it is indirectly sensitive to both the forces and distances between atoms or molecules. The advantage of acoustic imaging in comparison to optical imaging based on birefringence is straightforward: the optical properties are described by tensors of second order, whereas the acoustic properties are described by fourth order tensors. The latter have much higher information content because of the increased number of independent coefficients.

4.4. Determination of the elastic properties of soft polycrystalline materials

In sections 4.2 and 4.3, we evidenced that angle-resolved SBM^{θA} permits to probe the elastic properties of various structurally inhomogeneous or heterogeneous solids. As shown below, the SBM^{θA} technique also constitutes an elegant method to elucidate the elastic tensor properties of small crystal grains of polycrystalline films (KRÜGER *et al.* 1994, 2000, 2001). The elastic indicatrices just need to be measured within a sufficiently large number of differently oriented crystal grains in order to be able to estimate the elastic tensor components (see section 2.4) (KRÜGER *et al.* 2000, 2001). On the other hand, the use of polycrystalline films for the determination of the material's elastic tensor may be of interest if large single crystals are not available or if sufficiently large crystals are too soft to be cut into suitably oriented crystal slices (KRÜGER *et al.* 1994).

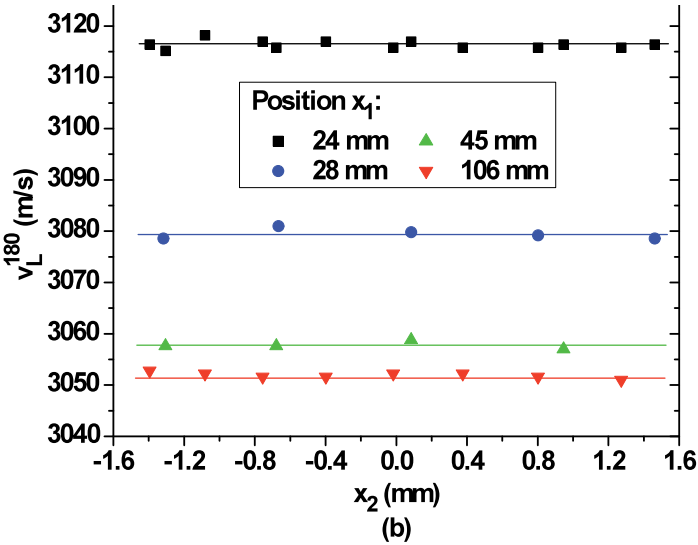
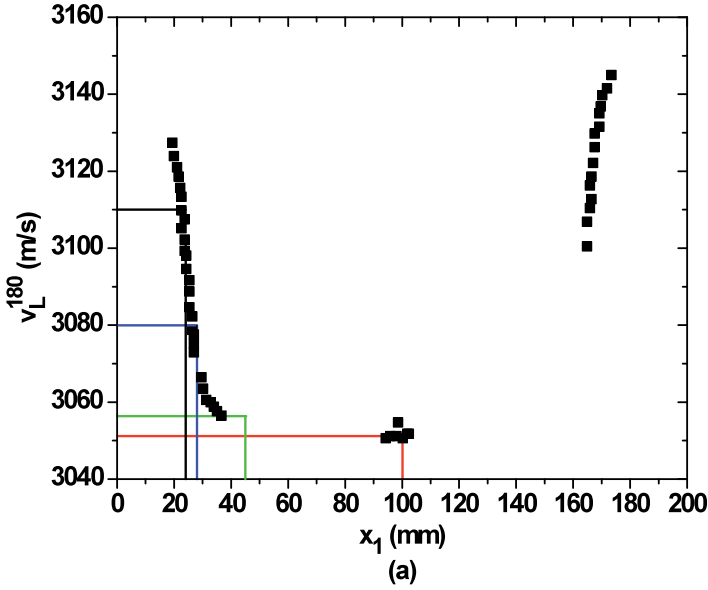


Fig. 4.9. Sound velocity v_L^{180} (a) versus the direction of stretching x_1 and (b) versus x_2 , with \vec{q}^{180} being parallel to \vec{x}_3 . Lines in figure (a): x_1 -positions for which the $v_L^{180}(x_2)$ -scans of figure (b) were made. Definition of coordinate system: see fig. 4.7.

In hard polycrystalline films, like the diamond plates discussed in section 4.5, optically visible boundaries or stress-induced birefringence may be indicative for grain boundaries. But be aware that if optical and elastic properties are not coupled, than these features can be misleading (KRÜGER *et al.* 2001). For films made of rather soft crystallites of cubic symmetry, optical birefringence may not exist at all. For such optically homogeneous polycrystalline films, SBM^{θA} constitutes an elegant recognition tool for the position and the size of arbitrarily oriented grains (KRÜGER *et al.* 1994). While scanning the scattering volume along an arbitrary trace, different sound velocities are actually recorded for each of the grains (possessing identical elastic tensor components) because of the different grain orientations!

This statement is demonstrated for a polycrystalline film consisting of symmetric difluorotetrachloroethane (DFTCE) in its plastic crystalline state, which looks optically as transparent and homogeneous as window glass (KRÜGER *et al.* 1994). The molecular crystal DFTCE has a melting temperature of about 299 K and crystallizes in cubic body centred symmetry (LOCKE *et al.* 1934). The investigated DFTCE sample's (and domains') thickness x_3 is about 30 μm (KRÜGER *et al.* 1994). Due to a proper adjustment of the 90A scattering geometry the constant phonon wave vector \vec{q}^{90A} is forced to lie in the (x_1, x_2) -plane of the sample (KRÜGER *et al.* 1994). The spatial variations of the quasi-longitudinal and quasi-transverse hypersonic velocities shown in figure 4.10 are probed along the same trace parallel to \vec{x}_1 . Figure 4.10a depicts the variations of the sound velocity of the quasi-longitudinally polarized phonon as a function of x_1 , suggesting the presence of three DFTCE domains along the 1.4 mm long scanning trace. The corresponding part of the much longer scanning trace of the quasi-transverse sound velocity indicated in figure 4.10b shows similar hypersonic features. For these hypersonic profiles of a polycrystalline DFTCE sample, a spatial resolution of about 50 microns is sufficient to substantiate the existence of domains with dimensions above half a millimetre (red guidelines). Originally figure 4.10 permitted to demonstrate that astonishingly large grain sizes of polycrystalline DFTCE films (KRÜGER *et al.* 1994) can be grown on highly oriented poly(tetrafluoroethylene) substrates (WITTMANN & SMITH 1991, KRÜGER *et al.* 1992, 1993, DAMMAN *et al.* 2001).

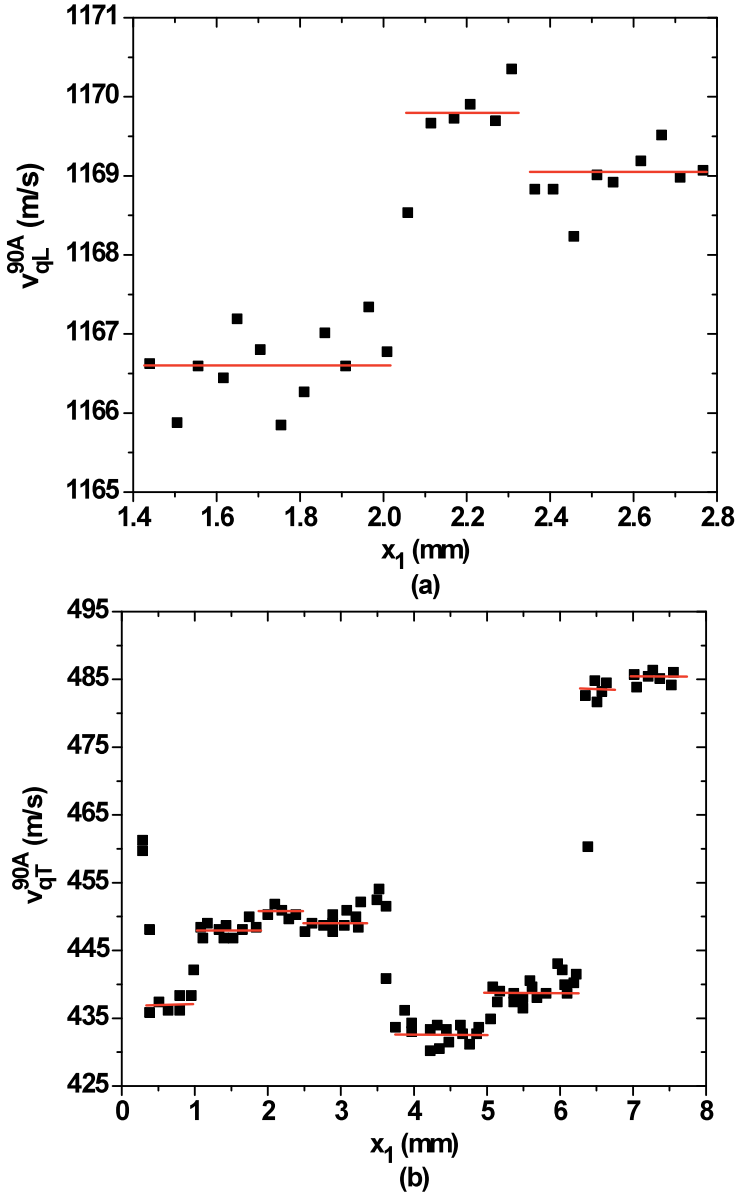


Fig. 4.10. Hypersonic velocity versus distance x_1 for (a) the quasi-longitudinally polarized mode and (b) the quasi-transversely polarized mode measured along the same trace at 290 K. Different domains are indicated by red guidelines.

4.5. Investigation of internal stress fields in polycrystalline diamond films

As elucidated in section 2.1, under thermodynamic equilibrium conditions BRILLOUIN spectroscopy probes second order elastic properties because of the involved small deformation amplitudes. If the second order elastic properties are modified by external stress fields, BRILLOUIN spectroscopy yields access to third order elastic moduli via the stress-induced changes of the second order elastic moduli (GRIMVALL 1986, KRÜGER *et al.* 1991). If a sufficient amount of external stress coefficients is known, than the implied third order elastic moduli can be determined. Similar to the case of external stress fields, the presence of an internal stress field in a material provokes that third order elasticity alters the second order elastic properties. The influence of internal stress fields on the elastic moduli is discussed in the following for small grain diamond plates. These plates can be treated as mechanically stressed materials of isotropic symmetry; one obtains according to (HUGHES & KELLY 1953):

$$c_L = c_{11} - \frac{\Delta p}{3c_{11} - 4c_{44}} (3c_{112} + 4c_{116} + 7c_{11} - 4c_{44}), \quad (4.5)$$

and

$$c_T = c_{44} - \frac{\Delta p}{3c_{11} - 4c_{44}} (3c_{166} + 4c_{456} + 3c_{11}), \quad (4.6)$$

where c_L and c_T represent the pressure modified equilibrium elastic moduli c_{11} and c_{44} . The third order moduli c_{ijk} with $i, j, k = 1, 2, \dots, 6$ are also written in VOIGT notation (KITTEL 2005), and Δp denotes the isotropic pressure. The differences $\Delta c_L = c_{11} - c_L$ and $\Delta c_T = c_{44} - c_T$ reflect the influence of the applied pressure on the equilibrium elastic moduli. The so-called stress coefficients Π_L and Π_T are approximated by (HUGHES & KELLY 1953):

$$\Pi_L \approx \frac{\Delta c_L}{\Delta p} = \frac{3c_{112} + 4c_{116} + 7c_{11} - 4c_{44}}{3c_{11} - 4c_{44}}, \quad (4.7)$$

and

$$\Pi_T \approx \frac{\Delta c_T}{\Delta p} = \frac{3c_{166} + 4c_{456} + 3c_{11}}{3c_{11} - 4c_{44}}. \quad (4.8)$$

The latter equations allow for estimating internal stress fields in polycrystalline diamond plates by approximating the local anisotropic stress field by a local pressure field $\Delta p_{L,T}(x_1, x_2, x_3)$ (KRÜGER *et al.* 2000, 2001). We obtain for the x_1 -direction:

$$\Delta p_L(x_1) \approx \frac{\Delta c_L(x_1)}{\Pi_L} \quad (4.9)$$

and

$$\Delta p_T(x_1) \approx \frac{\Delta c_T(x_1)}{\Pi_T}. \quad (4.10)$$

The study of residual stress fields within plates of chemical vapour deposited diamond having thicknesses of about 700 μm is presented below. Because of the chosen chemical vapour deposition process the diamond plates have quite different morphological, optical and mechanical properties on their nucleation side compared to the growth side. According to atomic force microscopy the lateral crystal dimensions are typically in the nanometer range on the nucleation side, whereas they amount up to 30 microns on the growth side (KRÜGER *et al.* 2000, 2001). The analysis of birefringence reveals that large mechanically stressed zones with an average diameter of several hundred micrometers exist throughout the diamond plates. The observed birefringence pattern does obviously not correlate with the crystalline grains as detected by atomic force microscopy. This discrepancy requires a quantitative and direct investigation of the internal stress fields by means of a sufficiently sensitive space-resolved elastic microscopy yielding the stress-induced changes of the elastic moduli field. The SBM ^{$\theta\Lambda$} -technique in combination with the RI $\theta\Lambda$ scattering geometry is perfectly adapted to this challenge and allows for successfully probing the internal stress fields at the nanocrystalline nucleation side as well as at the microcrystalline growth side of the diamond samples.

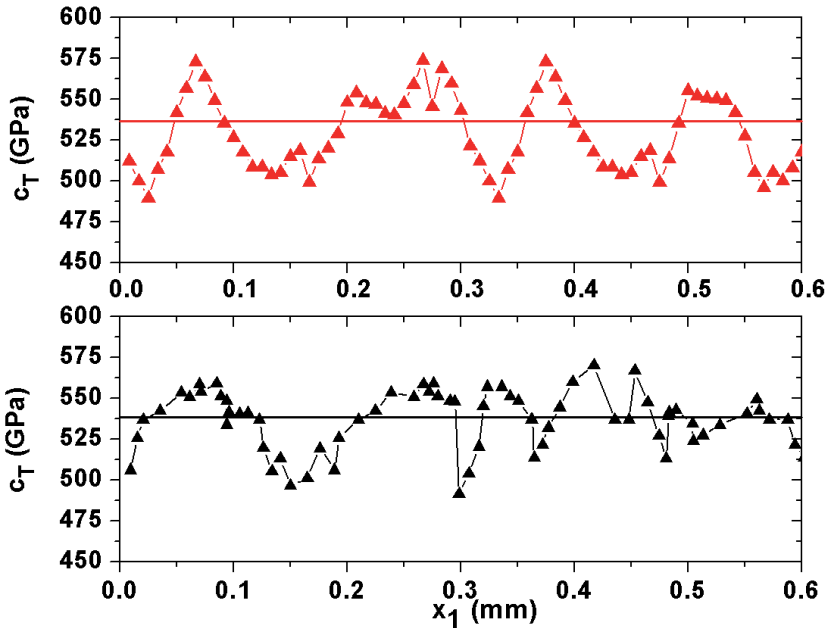


Fig. 4.11. Shear modulus c_T versus the position x_1 on the nanocrystalline nucleation side (in black) and on the microcrystalline growth side (in red) of a polycrystalline diamond plate. Horizontal lines: arithmetically averaged shear modulus value for both profiles.

Figure 4.11 gives the spatial variation of the shear modulus c_T along the x_1 -axis at the nucleation and growth sides of the polycrystalline diamond plate. The arithmetically averaged values of the measured shear moduli $\langle c_T \rangle_{x_1}$, indicated as solid lines in figure 4.11, are about 535 GPa on both sample sides. These values are close to the orientation average of the single crystal data for diamond, provided that the VOIGT model (constant strain condition!) is used (KRÜGER *et al.* 2001). The maximum deviation of $c_T - \langle c_T \rangle_{x_1}$ is almost about 10% and hence much bigger than the instrumental accuracy of BRILLOUIN spectroscopy, which lies below one percent. As furthermore the typical length scale of the shear modulus variations on the x_1 -axis is much larger than the grain sizes, these deviations are attributed to the presence of local internal stress fields influencing the elastic moduli.

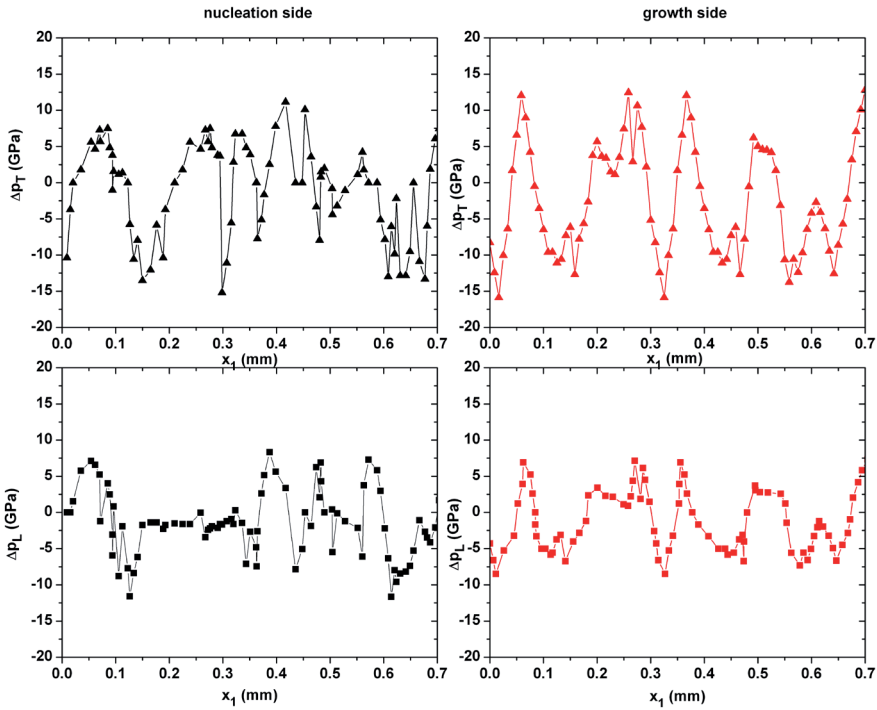


Fig. 4.12. Residual stresses on the nanocrystalline nucleation side (in black) and on the microcrystalline growth side (in red) of a diamond plate determined in RI θ A scattering technique.

Based on this assumption, we estimated the local internal pressure $\Delta p_T(x_1)$ by inserting into equation (4.10) the stress coefficient $\Pi_T = 2.98$ for diamond single crystals (MCSKIMIN & ANDREATCH 1972, GRIMSDITCH & RAMDAS 1975, ANASTASSAKIS *et al.* 1990) and the experimental data given in figure 4.11. For the sake of completeness the local internal pressure for the longitudinal acoustic mode $\Delta p_L(x_1)$ is added to figure 4.12, using the stress coefficient $\Pi_L = 5.98$ (MCSKIMIN & ANDREATCH 1972, GRIMSDITCH & RAMDAS 1975, ANASTASSAKIS *et al.* 1990). According to figure 4.12, stress components of several GPa are observed within the diamond plate independent of the polarization of the acoustic mode. The

internal stress fields strongly vary over distances of about hundred microns. Most astonishing is the fact that no clear difference can be evidenced between the elastic data recorded on both sides of the diamond plate: the spatial variations of the internal stress fields indeed behave similarly on the nanocrystalline and on the microcrystalline sides. This result suggests that there is almost no effect of the grain size and the grain boundaries on the internal stress fields. The internal stress fields are hence of long-range order and rather uniformly distributed throughout the polycrystalline diamond plate. This observation confirmed earlier results achieved by much more indirect probes like x-ray scattering (CLAUSING *et al.* 1991) and RAMAN spectroscopy (VLASOV *et al.* 1997).